JOURNAL OF GEOPHYSICAL RESEARCH, VOL. 99, NO. D12, PAGES 25,819–25,833, DECEMBER 20, 1994

Global-scale modes of surface temperature variability on interannual to century timescales

Michael E. Mann and Jeffrey Park

Department of Geology and Geophysics, Yale University, New Haven, Connecticut

Abstract. Using 100 years of global temperature anomaly data, we have performed a singular value decomposition of temperature variations in narrow frequency bands to isolate coherent spatio-temporal "modes" of global climate variability. Statistical significance is determined from confidence limits obtained by Monte Carlo simulations. Secular variance is dominated by a globally coherent trend, with nearly all grid points warming in phase at varying amplitude. A smaller, but significant, share of the secular variance corresponds to a pattern dominated by warming and subsequent cooling in the high latitude North Atlantic with a roughly centennial timescale. Spatial patterns associated with significant peaks in variance within a broad period range from 2.8 to 5.7 years exhibit characteristic El Niño-Southern Oscillation (ENSO) patterns. A recent transition to a regime of higher ENSO frequency is suggested by our analysis. An interdecadal mode in the 15-to-18 years period range appears to represent long-term ENSO variability. This mode has a sizeable projection onto global-average temperature, and accounts for much of the anomalous global warmth of the 1980s. A quasi-biennial mode centered near 2.2-years period and a mode centered at 7-to-8 years period both exhibit predominantly a North Atlantic Oscillation (NAO) temperature pattern. A potentially significant "decadal" mode centered on 11-to-12 years period also exhibits an NAO temperature pattern and may be modulated by the century-scale North Atlantic variability.

1. Introduction

In the face of possible anthropogenic effects on global climate, there is a need to characterize better the nature of historical climate variability. Aside from possible episodic volcanic forcing [e.g., *Bradley and Jones*, 1992], organized interannual climate variability seems to be associated largely with the El Niño-Southern Oscillation (ENSO) [e.g., *Philander*, 1990], the quasi-biennial oscillation (QBO) [e.g., *Trenberth and Shin*, 1984], and regional climate processes, such as the North Atlantic Oscillation (NAO) [e.g., *Bjerknes*, 1964; *van Loon and Rogers*, 1978; *Rogers*, 1984; *Lamb and Peppler*, 1987] which may have hemisphere- or even global-scale influence. Decadal and interdecadal variability is less well understood and has variously been attributed to internal variability in the thermohaline circulation of the oceans [*Levitus*, 1989; *Ghil and Vautard*, 1991; *Stocker and Mysak*, 1992; *Read and Gould*, 1992], coupled cryosphere-ocean-atmosphere cycles [*Mysak and Power*, 1992], and external astronomical forcing due to the 18.6-year soli-lunar tide [*Currie and O'Brien*, 1992; *Mitra et al.*, 1991], the ~11-year solar cycle [*Labitzke and van Loon*, 1988; *Mitra et al.*, 1991; *Currie and O'Brien*, 1992] and its 22-year subharmonic or "Hale" cycle [*Vines*, 1986]. On century and longer timescales, thermohaline and cryosphere variability [*Stocker and Mysak*, 1992], solar forcing [*Friis-Christensen and Lassen*, 1991], and anthropogenic factors [e.g., *International Panel on Climate Control (IPCC)*, 1990] have been argued to be important.

While there is scant evidence for truly periodic historical interannual climate signals (that is, phase-coherent sinusoidal variations) there is nonetheless strong evidence that certain climatic processes are quasi-periodic. Such processes exhibit well-defined timescales of oscillation but are frequency or amplitude modulated on a longer timescale, often in an unpredictable manner. Thus spectral energy is spread out in a finite band about some dominant frequency. For example, ENSO variability appears to concentrate into distinct low-frequency (4-6 year) and high-frequency (2-3 year) bands [e.g., *Barnett*, 1991; *Keppenne and Ghil*, 1992; *Dickey et al.*, 1992; *Ropelewski et al.*, 1992]. Quasi-periodic modes of climate variability, then, should be identifiable as statistically significant, relatively narrowband peaks in the spectra of global climate records. Any global modes of climate variability should also be associated with spa-

Paper number 94JD02396.
0148-0227/94/94JD-02396$05.00

tially coherent patterns arising from "teleconnections" between distant regions, and it is thus important to analyze historical data in a manner that investigates both the spectral and spatial character of climate variations.

Although the geopotential height field might be the most instructive to analyze for climatic variability, the records only go back about 50 years. Long records of sea level pressure are available but are largely confined to the northern hemisphere. Long and widespread records of precipitation exist, but they represent a more indirect proxy for underlying underlying physical processes. Surface temperature anomaly records [*Jones et al.*, 1986a, b, c; *Hansen and Lebedeff*, 1987; *Jones and Briffa*, 1992] provide reasonably global, if sparse, coverage since about 1890, and their variability have been successfully correlated with that of geopotential heights and SLP [e.g., *van Loon and Rogers*, 1976; *Trenberth*, 1990; *Palecki and Leathers*, 1993], suggesting that temperature data might serve as a useful indicator of variability in global atmospheric circulation patterns, as well as in the net surface heat budget.

Several workers [*Folland et al.*, 1984; *Kuo et al.*, 1990; *Ghil and Vautard*, 1991; *Elsner and Tsonis*, 1991; *Allen et al.*, 1992] have examined records of global- and hemisphere-averaged land air and/or sea surface temperature records for signals on interannual to century timescales. *Mann and Park* [1993] demonstrated that interdecadal temperature signals, while widely correlated, exhibit spatial variability that leads to considerable cancellation in a global average. Therefore an analysis only of modes which have large projection onto global-average temperature gives an incomplete picture of global-scale variability. In the present study we thus seek to isolate the spatial structure of modes of climatic variability, including those whose effect is largely to redistribute heat over the Earth's surface. Such an approach provides some insight into the nature of the underlying climatic processes. Similar approaches, based on a variety of climatic indices, have been applied on a regional basis [*Dickson and Namias*, 1976; *Dettinger and Ghil*, 1991; *Cayan and Peterson*, 1989; *Lins*, 1985; *Currie and O'Brien*, 1992] or on a global basis, but with relatively shorter records [*Xu*, 1993], or for particular phenomena such as ENSO [*Ropelewski and Halpert*, 1987; *Bradley et al.*, 1987; *Halpert and Ropelewski*, 1992; *Barnett*, 1991]. Longer-term variations over several centuries have also been studied using a combination of proxy and historical temperature data [*Bradley and Jones*, 1993]. To the best of our knowledge, however, there are no previous studies using records of sufficent duration and global extent to characterize modes of global climatic variability through interdecadal time scales.

In this paper we describe the application of a singular value decomposition (SVD) analysis of historical gridded surface temperature anomalies simultaneously in the spectral and spatial domains to investigate the timescale, spatial pattern, and temporal evolution of potential quasi-periodic modes of climate variability. We isolate statistically significant spatio-temporal "signals" by comparing their explained variance to that expected from the random fluctuations of independent, uncorrelated time series. To estimate how many effectively uncorrelated regions, or spatial degrees of freedom $\tilde{M}$, are represented in our spatial sampling of the temperature field, we estimate a characteristic near-neighbor correlation length of temperature fluctuations which, in constrast to weaker long-range correlations, is largely independent of the timescale of analysis. We test for "signals" against the null hypothesis that observed temperature fluctations arise from random fluctuations of a set of $\tilde{M}$ data series. We describe the temperature data set and the SVD analysis in the next two sections and subsequently the results of our analysis.

2. Data

The data used consists of land air and sea surface temperature anomalies distributed on a $5° \times 5°$ global grid [see *Jones and Briffa*, 1992]. To obtain nearly continuous monthly sampling from 1891 to 1990, we use a subset consisting of $M = 449$ grid points containing only small gaps (less than 6 months). We interpolated these gaps linearly, yielding time series of length $N = 1200$ months (i.e., 100 years). Such interpolation is defensible in this context as we restrict our attention to variability on timescales $\tau > 2$ years. Potential sources of bias in the data include corrections for urban warming, historical changes in data collection, and the weighting of data within grid points. We do not address these issues here but rather refer the reader to other detailed discussions [*IPCC*, 1990, chapter 7; *Jones and Briffa*, 1992]. We note that many such sources of bias should have diminished influence in our search for quasi-periodic, spatially coherent variations. Episodic effects such as volcanic forcing and isolated regional variability are likely to be treated as "noise" in our analysis, unless such forcing amplifies the variance in other climatic processes.

Because the data samples the Earth's surface unevenly, poorly sampled regions (e.g., high southern latitudes) may be weakly represented in the analysis, while well-sampled regions (e.g., northern Europe) may exert influence out of proportion with their true priority in the global climate system. No climate data sets of significant length are, however, free from this shortcoming. The effective spatial degrees of freedom $\tilde{M}$ in the data set is far less than the aggregate number M of grid points. In fact, $\tilde{M}$ is properly considered a function of the timescale under consideration [e.g., *Briffa and Jones*, 1993], principally because enhanced long-range teleconnections tend to decrease $\tilde{M}$ on interannual and longer timescales. Keeping this in mind, *Mann and Park* [1993] estimated a short-range, near-neighbor correlation length between grid points of roughly $d = 1500$ km, which we have refined to $d \approx 2000$ km, that is essentially independent of timescale. In such an estimate, assumptions of homogeneous and isotropic spatial behavior are necessarily invoked which are not wholly justifi-

able [e.g., *Julian and Thiebaux*, 1975; *Kim and North*, 1991]. Distinctions in d exist between winter and summer seasons, [*Livezey and Chen*, 1983]. and our analysis should be influenced more heavily by winter variability. Our estimate of d is consistent with the range of values determined in other previous calculations based on observational and modeled data [*Kim and North*, 1991; *Madden et al.*, 1993]. We obtain an estimate of $\tilde{M} \approx 40$ equal-area rectangles of side d required to cover all sampled regions (see Figure 1). However, since our analysis is weighted by the most highly sampled regions, a more conservative estimate includes only rectangles with relatively dense coverage (e.g., containing 10 or more grid points) giving a value $\tilde{M} \approx 20$. In what follows we adopt confidence limits (Appendix C) based on Monte Carlo simulations with the more conservative estimate of $\tilde{M} = 20$ spatial degrees of freedom. An alternative resampling experiment, also described in Appendix C, suggests more liberal bounds. However, all of the above choices lead to the same group of signals that are significant at $\gtrsim$95% confidence.

3. Methods

For each grid point time series we remove the long-term (100 year) mean before analysis. The annual cycle has already been removed from the *Jones and Briffa* [1992] temperature anomaly data set. To assure that regions with high variance (e.g., centers of continents) do not dominate the SVD analysis, we normalize each grid point time series $\{x'_n\}^{(m)}$ by its standard deviation $\sigma^{(m)}$, where $n = 1, \ldots, N = 1200$ months. This normalization focuses our analysis toward large-scale coherent patterns, rather than local, perhaps high amplitude, variability. It also weights the analysis toward the winter season during which synoptic variance is greater. In order to study quasi-periodic phenomena, we transform the grid point series from the time to spectral domain using the multitaper spectral representation [*Thomson*, 1982; *Park et al.*, 1987; *Vernon et al.*, 1991]. Given the set of normalized time series ${x_n}^{(m)} = {x'_n}^{(m)}/\sigma^{(m)}$ we calculate the tapered Fourier transforms at a given frequency f,

$$Y_l^{(m)}(f) = \sum_{n=1}^{N} w_n^{(l)} {x_n}^{(m)} e^{i2\pi f n \Delta t} \tag{1}$$

where $\Delta t = 1$ month is the sampling interval. The data taper $\{w_n^{(l)}\}_{n=1}^{N}$ is the lth member in an orthogonal sequence of K Slepian tapers determined by a variational condition to minimize spectral leakage outside a chosen frequency interval. Using the definitions of *Thomson* [1982], $\left|Y_l^{(m)}(f)\right|^2$ is the lth eigenspectrum estimate of the normalized time series $\{x_n^{(m)}\}$ at frequency f.

The Slepian data tapers are mutually orthogonal, which leads to the property that the spectral estimates $Y_l^{(m)}(f)$, $l = 0, \ldots K-1$ are statistically independent, allowing multiple degrees of freedom within a given narrow frequency band. This is the main rationale for using the multitaper technique, as most standard techniques lead to spectral estimates (e.g., adjacent values of a fast Fourier transform) that are statistically correlated. A set of tapers that have energy concentrated within a half-bandwidth of pf_R are denoted as $p\pi$-prolate Slepian tapers, where $f_R = (N\Delta t)^{-1}$ is the Rayleigh frequency. The analysis is performed at each frequency point in the discrete Fourier transform. Spectral fluctuations over a frequency width narrower than f_R are generally not resolvable. The number of tapers K represents a compromise between the variance and frequency resolution of the Fourier transforms. The Slepian tapers average over a half-bandwidth of pf_R, and only the first $K = 2p-1$ tapers are usefully resistant to spectral leakage. We choose $p = 2$ and $K = 3$, these being the maximum values that provide multiple spectral degrees of freedom with sufficiently narrow frequency resolution to resolve both interdecadal and secular variance in the frequency domain. A parallel analysis with $p = 3$ and $K = 5$ was performed for comparison. The set of K tapered eigen-

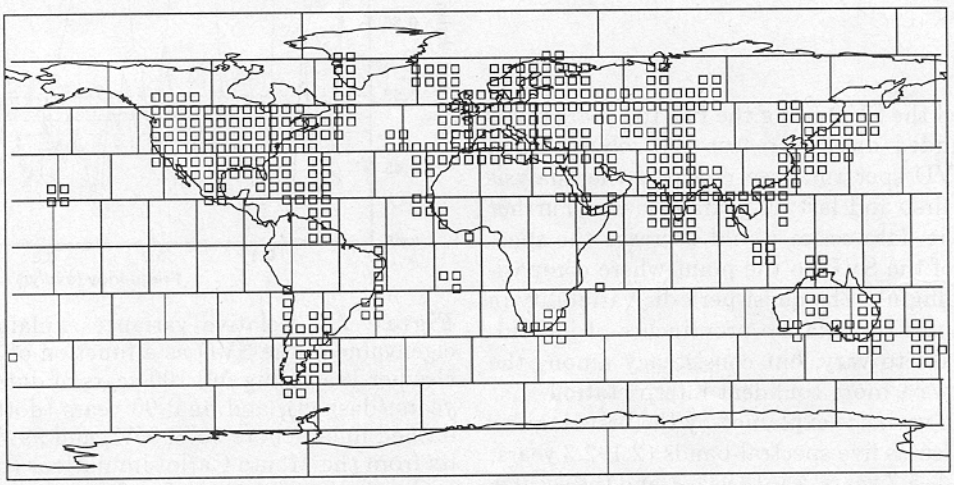

Figure 1. Locations of grid points used in analysis, indicated by small boxes. A coarser grid of 2000 km x 2000 km indicates roughly independent spatial regions.

spectra at a given frequency f represent statistically independent local averages of the spectral information near f, under the assumption that the time series analyzed exhibit a "locally white" spectral background. This is a good approximation for the data series used here (see Appendix C).

To decompose narrowband signals, we form the $M \times K$ matrix,

$$\mathbf{A}(f) = \begin{bmatrix} Y_1^{(1)} & Y_2^{(1)} & \dots & Y_K^{(1)} \\ Y_1^{(2)} & Y_2^{(2)} & \dots & Y_K^{(2)} \\ \vdots & & & \\ Y_1^{(M)} & Y_2^{(M)} & \dots & Y_K^{(M)} \end{bmatrix} \quad (2)$$

each row calculated from a different grid point time series, each column using a different Slepian taper, and we perform the complex singular value decomposition [e.g., *Marple*, 1987] of the above matrix,

$$\mathbf{A}(f) = \sum_{k=1}^{K} \lambda_k(f)\mathbf{u}_k(f) \otimes \mathbf{v}_k^*(f) \quad (3)$$

into K orthonormal left-eigenvectors $\mathbf{u}_k$, representing empirical orthogonal functions (EOFs) in the spatial domain, and K orthonormal right-eigenvectors $\mathbf{v}_k$, representing EOFs in the spectral domain. The asterisk denotes complex conjugation, while the $\otimes$ symbol represents the tensor, or outer, product between two vectors. The $\mathbf{v}_k$ are complex-valued K vectors and can be inverted (Appendix A) to obtain the slowly varying envelope of the kth mode of variability near frequency f. The $\mathbf{u}_k$ are complex-valued M vectors which determine the spatial pattern (amplitude and relative phase) of temperature variations among grid points associated with the kth mode of variability (Appendix B). The singular value $\lambda_k(f)$ scales the amplitude of the kth mode. We order the singular values $\lambda_1(f) \geq \lambda_2(f) \geq \ldots \geq 0$. The fractional variance explained by the kth mode within a given band, $\lambda_k^2 / \sum_{j=k}^{K} \lambda_j^2$ can be compared with confidence limits obtained by Monte Carlo simulations (Appendix C) to estimate statistical significance.

4. Results

We performed the SVD using the full 100 years (1200 months) of gridded data. To test the robustness of peaks in the SVD spectrum, we repeated the analysis using only the first and last 90 years of data. Further truncation of the data series would decrease the spectral resolution of the SVD to the point where comparison is not meaningful. The quasi-periodic variability in the data set causes the relative prominence of individual spectral peaks to vary, but consistency among the three trials allows a more confident interpretation.

The fractional variance explained by the first singular value $\lambda_1(f)$ indicates five spectral bands (2.1–2.3 years, 4.3–4.8 years, 5.1–5.7 years, 15–18 years, and the secular band) where the fractional variance breaches the 99% confidence level for nonrandomness in each of the three trials (Figure 2). These likely correspond to meaningful signals. While the three eigenspectra average over a frequency interval $\Delta f = 0.04$ cycle/year, dominant variance within a band is rarely distributed uniformly among the tapers, so that the effective frequency resolution of the SVD can be somewhat higher. This explains the relative narrowness of several of the peaks shown. The peak near 2.8–3.0 years breaches the 99% confidence level in one of the three cases, and at least the 90% level in the other two. Peaks near 3.3–3.4 years, 7–8 years, and 11–12 years pass or nearly reach the 95% confidence level in two of the three cases, and at least the 90% confidence level in the remaining case. We interpreted these peaks as potentially meaningful and considered them further in our analysis. Several other peaks are less robust and were disregarded. The second singular value $\lambda_2(f)$ is not significant at any of the frequencies except in the secular band $f < 0.02$ cycle/yr, where the first two modes describe nearly all of the variance in the demeaned data series. With $K = 3$ eigenspectral estimates, determining the significance of λ_2 in the secular band is complicated by the fact that $\lim_{f \to 0} \lambda_3 = 0$ for demeaned time series. The significance of λ_2 in this case is confirmed by the fact that the associated mode is found to be statistically significant in a parallel analysis with $K = 6$ Slepian tapers with time-bandwidth product $p = 4$. We conclude that there are 10 potentially significant spatio-temporal signals present in the global surface temperature anomaly record. Peaks in fractional variance near 15-to-18-, 11-to-12-, and 7-to-8-years period are well separated and can be associated with distinct "modes" of variability. Higher frequency peaks, particularly within the low frequency 4-to-6-years ENSO band, are more broadband in nature, so that the enumeration of "modes" is somewhat arbitrary. It is nonetheless useful to examine

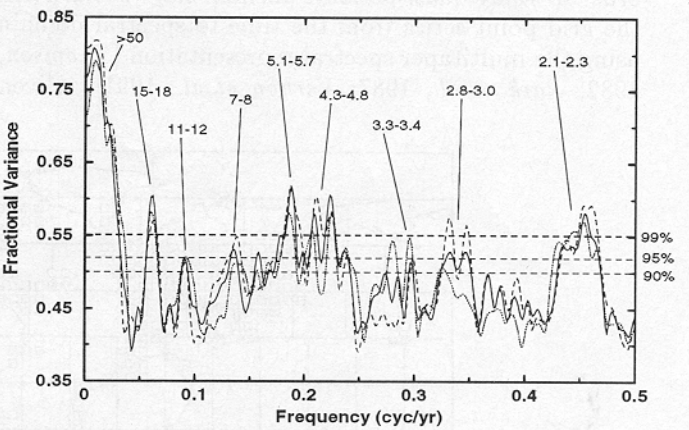

Figure 2. Relative variance explained by the first eigenvalue of the SVD as a function of frequency in cycles per year using full 100 years of data (solid), first 90 years (dashed), and final 90 years (dotted). Horizontal dashed lines denote 90%, 95%, and 99% confidence limits from the Monte Carlo simulations (confidence limits within the secular band $f < 0.02$ cycle/yr are somewhat higher; see Table C1). Significant peaks are labeled with approximate timescales in years.

Table 1. Statistically Significant Spatio-Temporal Signals Isolated in the SVD Analysis, Enumerated in Order of Increasing Frequency, Along With Associated Range in Frequency and Period of the Signal, Fractional Variance of the Associated Frequency Band Explained, Maximum Amplitude Regional Variability in Pattern, Root-Mean-Square Variability in Pattern, Average Variability in Pattern, and Projection of Pattern Onto Global-Average Temperature

	f (cycle/yr)	τ (years)	% Variance	T_{MAX}	T_{RMS}	T_{GLB}	P_{GLB}
1	0–0.02	>100	0.77	1.7	0.55	0.51	0.94
2	0–0.02	~100	0.23	1.4	0.29	0.03	0.10
3	0.055–0.065	15–18	0.60	1.6	0.45	0.18	0.40
4	0.085–0.09	10–12	0.52	1.7	0.37	0.06	0.17
5	0.13–0.15	6.7–7.7	0.53	1.4	0.39	0.16	0.42
6	0.175–0.195	5.1–5.7	0.62	1.6	0.36	0.09	0.32
7	0.21–0.23	4.3–4.8	0.61	1.6	0.37	0.15	0.41
8	0.295–0.30	3.3–3.4	0.51	1.3	0.36	0.10	0.28
9	0.32–0.35	2.8–3.0	0.53	1.1	0.28	0.11	0.40
10	0.43–0.47	2.1–2.3	0.58	1.5	0.38	0.14	0.36

Amplitudes of variability (in Celsius) correspond to maximum amplitude of the envelope of the corresponding quasi-periodic oscillation.

seperately the high- and low-frequency ENSO peaks, which we loosely refer to as ENSO "components," as well as the variability associated with the 2.1-to-2.3 year quasi-biennial band. In each case our determination of spatio-temporal patterns is based on performing the SVD at the central frequency of a given peak of interest.

As a crosshcek, we performed a parallel analysis to estimate the effect of variable sampling density using a small subset ($M = 50$) of grid points scattered nearly uniformly over the globe. The resulting SVD spectrum was quite similar to that obtained with the full ($M = 449$) sampling. The most noteable differences are greater prominance of the 2-to-3-years timescale ENSO peaks, and a slight shift of the quasi-decadal peak towards higher frequency (centered closer to 10 than 11 years period in this case). We conclude that the SVD analysis is fairly robust to variations in spatial sampling density (e.g., the large number of grid points surrounding the North Atlantic). The bias introduced by the sparseness of our data set itself, however, is difficult to determine. *Mann and Park* [1994] estimated the spectral coherence between northern and southern hemisphere-averaged temperature anomalies [*Jones et al.*, 1986a, b, c] and found statistically significant correlation in each of the bands noted in Figure 2, with the exception of the 5-to-6-years and 11-to-12-years variability. Both of these timescales display weaker amplitude in the southern hemisphere, as shown below.

Table 1 itemizes the 10 signals isolated by the SVD analysis. Table 2 indicates the temporal and spatial correlation between distinct modes. See Appendix B for precise definitions of the tabulated quantities. The quantitative comparisons corroborate a qualitative inspection of the temperature patterns. Patterns of temperature variability near 2.8-to-3.0-, 3.3-to-3.4-, 4.3-to-4.8-, and 5.1–5.7-years period share the characteristic ENSO spatial pattern of sizeable, in-phase variability throughout the tropics, with dipole and quadropole pat-

Table 2. Squared Correlations (Fraction of Shared Variance) Associated With Distinct EOF Pairs Assuming 20 Complex Spatial and 3 Complex Spectral Degrees of Freedom

τ, years	> 100	≈ 100	$15-18$	$10-12$	$7-8$	$5.1-5.7$	$4.3-4.8$	$3.3-3.4$	$2.8-3.0$	$2.1-2.3$
> 100	1	0	0.16	0.13	0.44	0.33	0.25	0.19	0.10	0.77*
≈ 100	0	1	0.67	0.87*	0.11	0.51	0.49	0.54	0.30	0.21
$15-18$	0.13†	0.03	1	0.54	0.13	0.44	0.81*	0.95‡	0.52	0.15
$10-12$	0.00	0.06	0.37‡	1	0.25	0.55	0.23	0.38	0.40	0.44
$7-8$	0.13†	0.01	0.01	0.10	1	0.51	0.05	0.22	0.16	0.70†
$5.1-5.7$	0.04	0.04	0.25‡	0.22‡	0.03	1	0.20	0.27	0.04	0.70†
$4.3-4.8$	0.08	0.04	0.22‡	0.01	0.04	0.33‡	1	0.81*	0.25	0.04
$3.3-3.4$	0.07	0.02	0.25‡	0.16*	0.09	0.34‡	0.32‡	1	0.56	0.09
$2.8-3.0$	0.13†	0.01	0.11†	0.02	0.13†	0.25‡	0.42‡	0.25‡	1	0.07
$2.1-2.3$	0.02	0.01	0.05	0.26‡	0.17*	0.06	0.11†	0.19*	0.08	1

The top triangle compares spectral EOFs or spectral "envelopes" for different signals (identified by their periodicity in years as given in Table 1). The bottom triangle compares the spatial EOFs for different signals.

*= > 95%
†= > 90%
‡= > 99%

terns of warming or cooling in the extratropics that suggest the influence of established teleconnection patterns such as Pacific North American (PNA) or Tropical Northern Hemisphere (TNH), NAO, Western Pacific Oscillation (WPO) and perhaps others [see *Wallace and Gutzler*, 1981; *Barnston and Livezey*, 1987] The spatial EOFs associated with each of these peaks are correlated at greater $> 99\%$ confidence level, with $|(\mathbf{v}_1(f))^* \cdot \mathbf{v}_1(f')| > 0.5$ in each case. The spatial EOFs for 15-to-18- and 11-to-12-years periods correlate with the 3.3-to-3.4- and 5.1-to-5.7-years ENSO spatial EOFs at >99% confidence. In this case each pattern appears to share both NAO and ENSO characteristics. Other groupings include spatial patterns associated with peaks centered at 2.1-to-2.3-, 7-to-8-, and 11-to-12-years period, which have high-amplitude NAO variability, with weaker tropical variability. While some correlations may be spurious, there are only 45 distinct correlation pairs, and very few should randomly exceed the 99% confidence level if $\tilde{M} \geq 20$.

4.1. Secular Modes

Two mutually orthogonal secular modes have substantial variance in the temperature data set. Spectral estimates at $f = 0$ average information from 0 to 0.02 cycle/yr and thus include variability on timescales $\tau \geq 50$ years. Higher frequency variability will not be contaminated by secular variations (to the extent that the three 2π-prolate Slepian tapers are optimized against spectral leakage). The primary secular mode (Figure 3) accounts for 77% of the low-frequency variance and is associated with a warming signal that projects strongly onto global temperature ($P_{\mathrm{GLB}} = 0.94$). Maximum regional warming (Table 1) is $\sim 1.7°$C, while the estimated global-average warming (see Appendix B) is closer to 0.5° C. The spatial pattern exhibits considerable variability, with certain grid points actually cooling slightly. Regional departures from the average warming of $\sim 0.5°$C suggest the presence of a positive PNA pattern (deficient warming in the southeastern United States coupled with enhanced warming in northwestern North America) and a WPO teleconnection pattern (enhanced warming in southeastern Asia coupled with weak warming farther north). It is possible that higher global temperatures may favor certain dynamical regimes of the climate system, such as PNA or WPO pressure anomalies. In fact, modeling experiments [e.g., *IPCC*, 1990, chapter 8; *Marshall et al.*, 1994] suggest that the fingerprint of anthropogenic warming may include such regional anomalies. The strongest warming ($\sim 1.7°$C) is observed along the margin of Greenland, which could indicate the influence of a positive ice-albedo feedback.

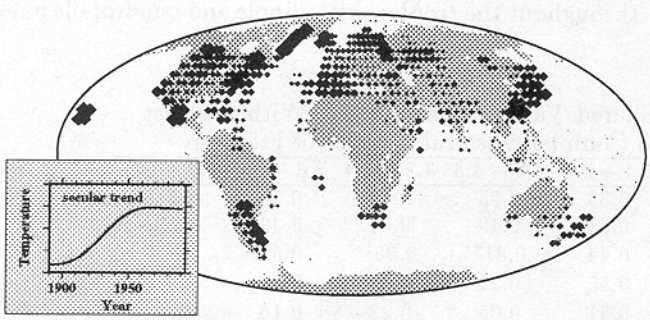

Figure 3. Spatial pattern of temperature variability associated with the first mode in the secular band 0-0.02 cycle/yr. Solid diamonds are used to indicate grid points evolving positively with the time domain signal shown in the inset (warming), while open circles represent the few grid points evolving negatively with the time domain signal shown (cooling). As in all subsequent plots, the symbol sizes scale the relative magnitude of temperature variations. The absolute scale for typical and maximum regional variations is indicated by Table 1.

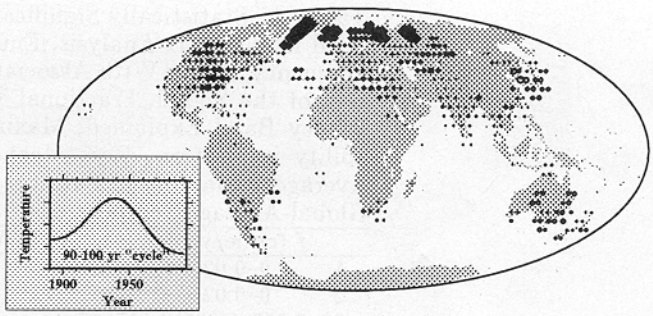

Figure 4. Spatial pattern of temperature variability associated with the secondary mode in the secular band. High-amplitude variability is confined largely to the North Atlantic. Each grid point evolves with the same 90−100 year "oscillation," shown in the inset, differing only in magnitude or sign. Solid diamonds evolve in phase with the North Atlantic, while grid points with open circles vary oppositely.

The time domain trend of the warming (inset, Figure 3) is roughly consistent with that obtained from globally averaged temperature anomalies [*Ghil and Vautard*, 1991] indicating gradual warming early in the period, rapid warming from 1930 until about 1950, and a cessation of warming thereafter. Because the trend is constrained primarily by our envelope inversion (Appendix A), extrapolation is perilous. For comparison, we computed the linear trend separately for each grid point. The results are quite similar to those above, albeit with a moderately higher prescribed warming ($T_{\mathrm{MAX}} = 1.87°$, $T_{\mathrm{RMS}} = 0.59°$, and $T_{\mathrm{GLB}} = 0.57°$). *Friis-Christensen and Lassen* [1991] have suggested a connection between secular warming and long-term variability in the ~11-years solar cycle (although no plausible physical mechanism was offered). We find no statistical evidence for such a connection, as the correlation between the warming mode and the envelope of the 11-years solar cycle in the spectral domain is not statistically significant (< 60% confidence level).

The remaining 23% of the secular variance displays a spatial pattern (Figure 4) with significant amplitude in the high-latitude North Atlantic (as large as 1.4°C, see Table 1), in-phase with smaller amplitude variability in the United States, Northern Europe, and the

Mediterranean region, and out of phase with variability elsewhere over the globe. The time domain signal (inset, Figure 4) suggests a 90-to-100-years "oscillation," but the timescale and oscillatory nature of such a mode is poorly constrained by the duration of the data set. The cycle of warming in the North Atlantic from roughly 1890-1940, and subsequent cooling, is consistent with the long-term trend in North Atlantic sea surface temperature and air temperatures determined elsewhere [*Deser and Blackmon*, 1991]. Concurrent work by *Schlesinger and Ramankutty* [1994], using a quite different methodology, demonstrates evidence for a 65-to-70-years oscillation in global temperatures, centered in the North Atlantic, which may also be related to our findings. Large temperature variations in the high-latitude North Atlantic supports a possible connection with century-scale variability in deep water production [e.g., *Stocker and Mysak*, 1992], and the opposite sign of anomalies in the North and South Atlantic is consistent with changes in the cross-equatorial heat-flux that would be expected to arise from variability in the thermohaline circulation. The near cancellation of the pattern in a global average suggests a process that largely redistributes heat over the Earth's surface.

4.2. ENSO

The SVD analysis confirms a rough division of ENSO variability into higher-frequency (2.8-to-3.0- and 3.3-to-3.4-years period) and lower-frequency (4.3-to-4.8- and 5.1-to-5.7-years period) bands. The spatial pattern (Figure 5) associated with the shortest-period ENSO spectral peak (2.8–3.0 years) is similar to the ENSO temperature pattern identified by *Halpert and Ropelewski* [1992]. Both patterns of temperature variability show roughly in-phase tropical warming coincident with warming and cooling, respectively, in the northwest and southeast United States. Such behavior is consistent with the positive phase of a PNA pattern that is known to accompany tropical warm events [*Horel and Wallace*, 1981]. Both patterns also share warming in eastern Europe coincident with cooling in central Asia and slight cooling in western Europe, as well as cooling in the northern Pacific in phase with warming in the tropical western Pacific. This latter pattern resembles the WPO teleconnection. Though much of ENSO warming is produced by tropical ocean-atmosphere heat exchange, some of this heat is transported poleward by a variety of processes. Hence there is a tendency for warming, for example, in middle as well as tropical latitudes even though anomalous advection can produce cooling in certain areas.

The other three ENSO spatial patterns share features of in-phase tropical warming with poleward teleconnections. A WPO temperature pattern in the North Pacific exists to varying degrees in each case, as well as PNA or TNH patterns in varying combinations. In each pattern, conditions are reversed for tropical warm and cold events. It is notable that the 5.1-to-5.7-years ENSO pattern (Figure 6) exhibits the most prominent NAO-type pattern of the four ENSO components identified,

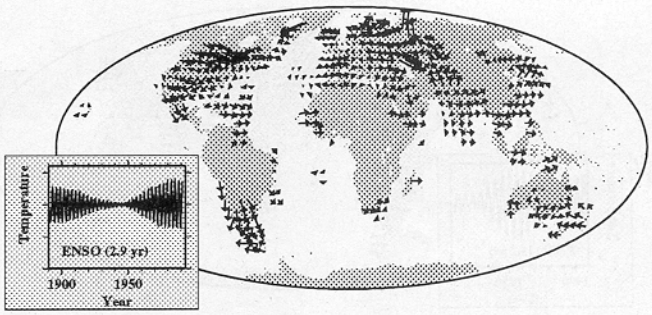

Figure 5. Spatial pattern associated with the 2.8-to-3.0-years ENSO component. The size of the vectors indicates relative magnitude of temperature variations. The absolute scale is provided by Table 2. Vector orientation indicates the relative temporal lag at each grid point. We define a zero phase vector (i.e., grid points with a vector pointing toward "3 o'clock," for example, much of the tropics in this case) as evolving positively with the time domain signal shown in the inset. Counterclockwise rotation in the spatial pattern indicates lag relative to zero phase. Clockwise rotation represents lead relative to zero phase. A rotation of 360 degrees corresponds to the periodicity of the mode ($\sim$ 2.9 years in this case). All grid points share the same oscillation envelope in the time domain, and the 2.9-years carrier oscillation shifts forward or backward with the phase lags indicated in the spatial pattern. For example, grid points with vectors at "12 o'clock" experience maximum warming at a 90° $\sim$ 0.7-year lag relative to peak tropical warming. Grid points at "6 o'clock" experience maximum warming at $\sim$ 0.7 year before peak tropical warming, and grid points at "9 o'clock" experience maximum cooling simultaneous with peak tropical warming. The pattern average variability is in phase with the tropical variability, so that peak projection onto global warmth corresponds to peak tropical warmth.

consistent with *Rogers* [1984] who found a peak near 6-years period in the cospectrum of the Southern Oscillation Index and NAO. As indicated in Table 1, the ENSO patterns all have considerable projections onto global temperature, each giving rise to $T_{GLB} \sim 0.10$°C. Other workers [*Jones*, 1989; *Angell*, 1990] have noted that ENSO leads to significant interannual variations in global average temperature. In each of our ENSO patterns, maximum global warm anomalies coincide with tropical warm events, while the maximum cold anomalies coincide with cold events.

The temporal evolution of the four distinct ENSO components (Figure 7) suggests a recent trend toward higher ENSO frequency, as the shorter-period components have tended to increase in amplitude over the last four decades, while the lower-frequency components have remained constant or diminished over the same period. This trend is interesting because it may have some bearing on theoretical speculation [e.g., *Palmer*, 1993] that decadal and longer timescale global climate change could influence the frequency of natural modes of the climate system, such as ENSO, that have a signficant projection onto global-average temperature.

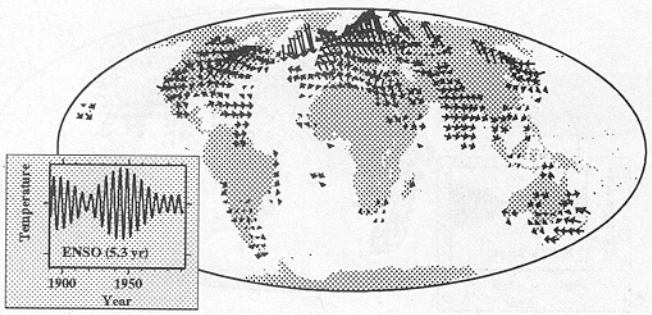

Figure 6. Spatial pattern associated with 5.1-to-5.7 years ENSO component, with zero phase (e.g., tropics) variability coincident with the time domain signal shown in the inset. Symbol conventions are identical to Figure 5.

4.3. Interdecadal Mode

An interdecadal mode (15–18 years) of temperature variability has a spatial pattern (Figure 8) consistent with that reported by *Mann and Park* [1993]. This mode may correspond to the bidecadal global temperature signal identified by *Ghil and Vautard* [1991] in global-average temperature. The spatial pattern resembles that of ENSO, with high-amplitude, in-phase tropical warming and extratropical variability consistent with teleconnections patterns such as PNA and NAO. Despite significant cancellation in the global average, this mode is associated with a sizeable peak-to-peak $T_{GLB} \sim 0.2°C$, with a maximum global warm anomaly coincident with tropical warming. The time domain signal (inset of Figure 8) suggests that the anomalous warmth of the 1980s was associated, at least in part, with a large positive excursion of the interdecadal oscillation. Note, however, that global warming in the interdecadal oscillation is associated with simultaneous cooling in the southeastern United States and Europe. If extrapolated one cycle forward, this interdecadal signal "predicts" anomalous coolness through the mid 1990s, with anomalous warmth, however, in the southeastern United States and Europe. The poor constraints on the secular warming mode near the endpoints of the data set limits the confidence of global temperature extrapolations. Any uncaptured recent acceleration of secular warming could overwhelm an opposing interdecadal variation.

In addition to spatial correlations at >99% confidence with three of the four ENSO spatial patterns, the interdecadal mode is significantly correlated with ENSO in the spectral domain, especially with the 3.3-to-3.4-years (99.8% level) and 4.3-to-4.8 years (>95%) ENSO components. This mode may thus represent ENSO variability on longer timescales. A connection between ENSO and interdecadal variability in the northern hemisphere has been suggested by previous work [*Trenberth*, 1990; *Tanimoto et al.*, 1993]. We also speculate that connections between global interdecadal variability and regional climate phenomena such as Sahel rainfall [*Folland et al.*, 1986], which are affected by ENSO [*Ropelewski and Halpert*, 1987], may relate to this signal. While thermohaline variability has been speculated to be important on interdecadal timescales [e.g., *Mysak and Power*, 1992], we find no obvious spatial features in the pattern that suggest such an origin. We have not investigated speculated relationships between interdecadal variability and the 18.6-year soli-lunar tide [e.g.,*Mitra et al.*, 1991; *Currie and O'Brien*, 1992].

4.4. Decadal Mode

A quasi-decadal mode of 10-to-12-years periodicity (Figure 9) exhibits a temperature pattern with weak projection onto global-average temperature ($P_{GLB} < 0.18$). The latter may explain why ~ 11-year variability is absent in analyses of globally averaged temperatures [*Folland et al.*, 1984; *Ghil and Vautard*, 1991] but emerges, for example, in regional studies of U.S.

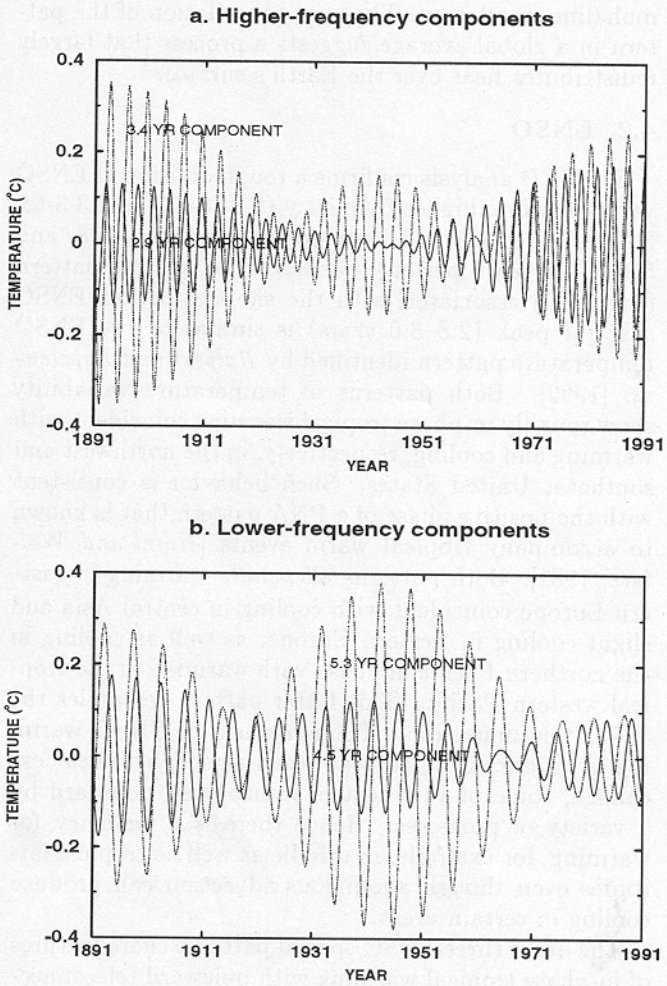

Figure 7. Time-domain signals associated with the various ENSO components, shown for a typical low-latitude grid point (containing Delhi, India) comparing (a) the higher-frequency (2.8-to-3.0-years, solid, 3.3-to-3.4-years, dotted) components. and (b) lower-frequency (4.3-to-4.8-years, solid, 5.1-to-5.7-years, dotted) components.

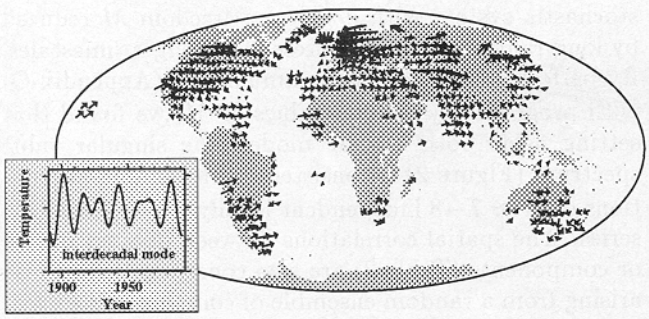

Figure 8. Spatial pattern associated with the 15-to-18-years interdecadal mode, with zero phase (e.g., tropics) evolving with the time domain signal shown in the inset. Maximum pattern average warmth is coincident with tropical warmth. Symbol conventions are similar to Figure 5.

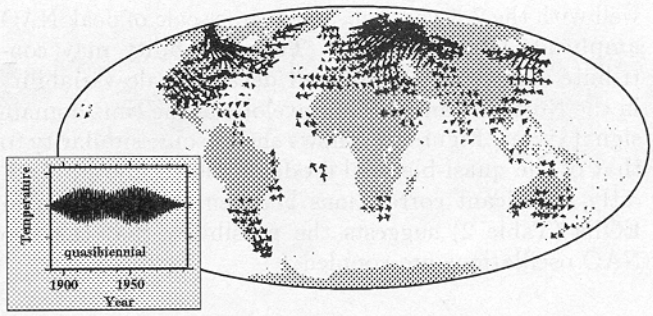

Figure 10. Spatial pattern of variability associated with the 2.1-to-2.3-years quasi-biennial mode. Zero phase variability (e.g., England) evolves positively with the time series shown in the inset. Symbol conventions are similar to Figure 5.

temperature [*Dettinger and Ghil*, 1991], precipitation [*Currie and O'Brien*, 1992] and Indian precipitation [*Vines*, 1986; *Mitra et al.*, 1991]. The spatial pattern is dominated by an NAO-type pattern with weaker tropical variability. There is some evidence (within the confines of our sparse sampling) of a dipole structure in the tropical Atlantic discussed elsewhere [e.g., *Houghton and Tourre*, 1992], as anomalies are roughly 180° out-of-phase just north and south of the equator. The envelope of the signal is significantly correlated (>95% confidence level) with the ~90-to-100-years secular variation described previously. Both patterns indicate high-amplitude variability in the North Atlantic, and it is possible that the underlying processes are coupled. The quasi-decadal signal is not significantly correlated (<50% confidence level) with the ~ 11-year sunspot cycle, which casts some doubt on speculation that solar forcing is significant on this timescale [e.g., *Currie and O'Brien*, 1992]. Other empirical evidence [*Deser and Blackmon*, 1991, 1993] and modeling experiments [e.g, *Weaver et al.*, 1991; *Mehta and Delworth*, 1994] suggest rather that internal ocean or ocean-atmosphere processes in the North Atlantic may be a source of decadal-scale climate variability.

4.5. Other Interannual Modes

A quasi-biennial (~ 2.2-year period) mode (Figure 10) is observed near the classical quasi-biennial oscillation (QBO) timescale. Consistent with observations of variability in winds, sea level pressures [*Deser and Blackmon*, 1991] and air temperatures [*Gordon et al.*, 1992] in the North Atlantic, and north-south variations in U.S. temperature [*Dettinger and Ghil*, 1991] on the same timescale, we observe a relatively prominant NAO temperature pattern connected with other extratropical regional anomalies. The pattern is associated with sizeable regional variations ($T_{\mathrm{RMS}} = 0.38°\mathrm{C}$), as well as a significant global average projection ($T_{AVE} = 0.14°\mathrm{C}$). Other workers have reported a QBO–ENSO connection [*Labitzke and van Loon*, 1988; *Barnston et al.*, 1991] associated with non-linear interaction of the QBO and low-frequency (i.e., 4-6 years) ENSO modes. We observe limited evidence for such a connection, as the spectral EOFs of the quasi-biennial and lowest-frequency ENSO modes are correlated near the 90% confidence level (Table 2). Such a marginally significant correlation, however, could well be spurious.

The timescale of the 7-to-8-years mode (Figure 11) which exhibits a prominent NAO pattern, corresponds

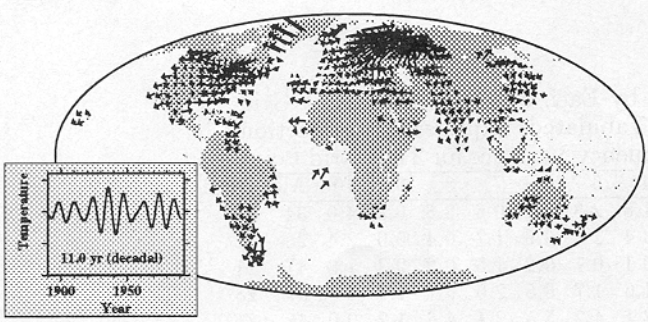

Figure 9. Spatial pattern of variability associated with the 10-to-12-years decadal mode, with zero phase variability (e.g., England, southeastern United States) evolving positively with the time series shown in the inset. Symbol conventions are similar to Figure 5.

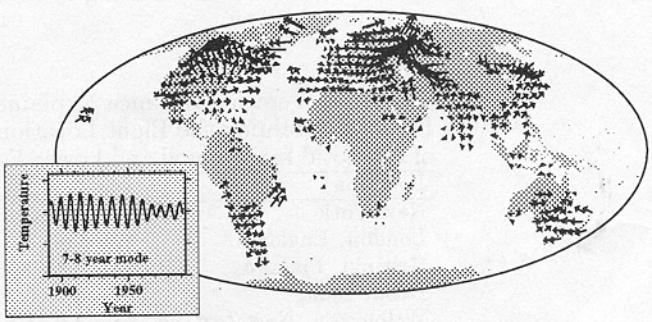

Figure 11. Spatial pattern of variability associated with the 7-to-8-years mode. Zero phase variability (e.g., England) evolves positively with the time series shown in the inset. Symbol conventions are similar to Figure 5.

well with the 7.3-years observed time scale of peak NAO amplitude [*Rogers*, 1984]. This variability may contribute somewhat to observed decadal-scale variability in the North Atlantic. The envelope of the time domain signal (inset, Figure 11) shows shows some similarity to that of the quasi-biennial mode discussed above. Modestly significant correlations between the two spectral EOFs (Table 2) suggests the possibility that the two NAO oscillations are coupled.

5. Discussion

It is informative to consider how well the 10 spatio-temporal signals isolated in our analysis explain temperature fluctuations at various locations over the globe. We indicate the fraction of total variance in the time series explained by each of the modes identified (Table 3) for eight example grid points. We also show how the reconstructed signal compares to the raw interannual variations at three of these grid points (Figure 12). Reconstructions based on all 10 signals identified describe between ~1% and ~75% of the interannual (i.e., $\tau >$ 2-years timescale) variance at particular grid points, and explain ~ 40% of the total interannual variance in the data set. The share of the variance, however, shrinks to a more modest 24% if secular variability is set aside. This leaves a large proportion of the interannual and longer variability in the global temperature data unexplained. ENSO variability exhibits a somewhat broadband character that may be incompletely captured by the four components identified in our analysis. Episodic volcanic forcing of climate [e.g., *Bradley and Jones*, 1992] and isolated regional variability (e.g., resulting from variations in local oceanic current systems) are possible sources of unexplained variance, as are any climatic "noise" or instrumental bias in records. It should not be surprising that a good deal of the historical temperature variance is not described well in terms of quasi-periodic variability. Lorenz, for example, has suggested that some interannual variability may be inherently chaotic [*Lorenz*, 1990].

We also investigated the extent to which the temperature variability can be viewed as resulting from a stochastic system with degrees of freedom $\tilde{M}$ reduced by long-range correlations present on longer timescales. By performing Monte Carlo simulations (Appendix C) with progressively smaller values of $\tilde{M}$, we found that setting aside both secular modes, the singular value spectrum (Figure 2) is consistent with random fluctuations of $\tilde{M} \approx 7-8$ independent locally white noise data series. The spatial correlations between distinct modes or components (Table 2) are also consistent with those arising from a random ensemble of complex-valued vectors with seven or eight components. Two conceptual models therefore appear consistent with the results of our study: (1) a collection of deterministic "signals" immersed in random fluctuations, and (2) stochastic variations of a climate system in which enhanced teleconnections at lower frequencies have reduced the effective spatial degrees of freedom to as few as 7 to 8. (The large unsampled region of the globe strongly suggests that this would be a lower bound on $\tilde{M}$.) From the narrow viewpoint of signal analysis, it is difficult to discriminate between the "deterministic" and "stochastic" conceptual models. However, the preferred timescales of climate processes such as ENSO, evidenced both empirically and theoretically, argue against a purely stochastic view of climate variability.

6. Conclusions

The spectral SVD technique implies a paradigm of a climate system whose fluctuations from a mean climate state operate largely through a small number of globally coherent processes, superimposed on a background of random regional and temporal variations. The true climate system is almost certainly more complex than this paradigm suggests. Nonetheless, a search for global-scale climatic processes that evolve in a quasi-periodic fashion provides considerable insight into historic climate variability.

Our analysis suggests that a significant share of climatic variability on interannual to century timescales may be associated with quasi-periodic processes of either external or internal origins. Organized interannual variability appears to be associated with ENSO,

Table 3. Percent Variance Explained by Each of the 10 Signals at Grid Points Containing the Eight Locations Tabulated, Expressed as a Fraction of the Total Interannual and Lower-Frequency Variance for That Grid Point

Location	1	2	3	4	5	6	7	8	9	10	All	DET
New York	18	0.4	1.0	1.8	2.8	2.7	0.6	2.5	0.3	4.0	34	19
London, England	7.2	0.8	0.3	3.4	2.2	9.6	1.7	0.4	0.0	2.4	28	22
Helsinki, Finland	34	7.4	1.7	0.1	0.1	0.2	1.5	0.9	0.3	1.8	47	11
Delhi, India	8.5	4.2	5.3	1.6	1.7	8.5	2.0	5.7	1.9	0.1	37	28
Wellington, New Zealand	18	2.9	4.5	2.1	4.2	5.5	2.1	4.6	1.2	0.0	45	31
East Coast Greenland	8.2	18	2.0	1.8	0.0	1.0	1.1	0.2	0.5	0.2	36	11
Santiago, Chile	5.4	4.3	5.6	0.8	4.0	0.7	8.0	1.1	6.1	0.8	35	28
Hawaii, Main Island	61	1.0	7.6	1.7	2.8	2.7	0.7	0.2	0.2	0.3	74	31

"All" indicates variance explained by all signals relative to total. "DET" indicates variance explained by interannual, decadal and interdecadal signals relative to detrended series, obtained by subtracting both secular modes.

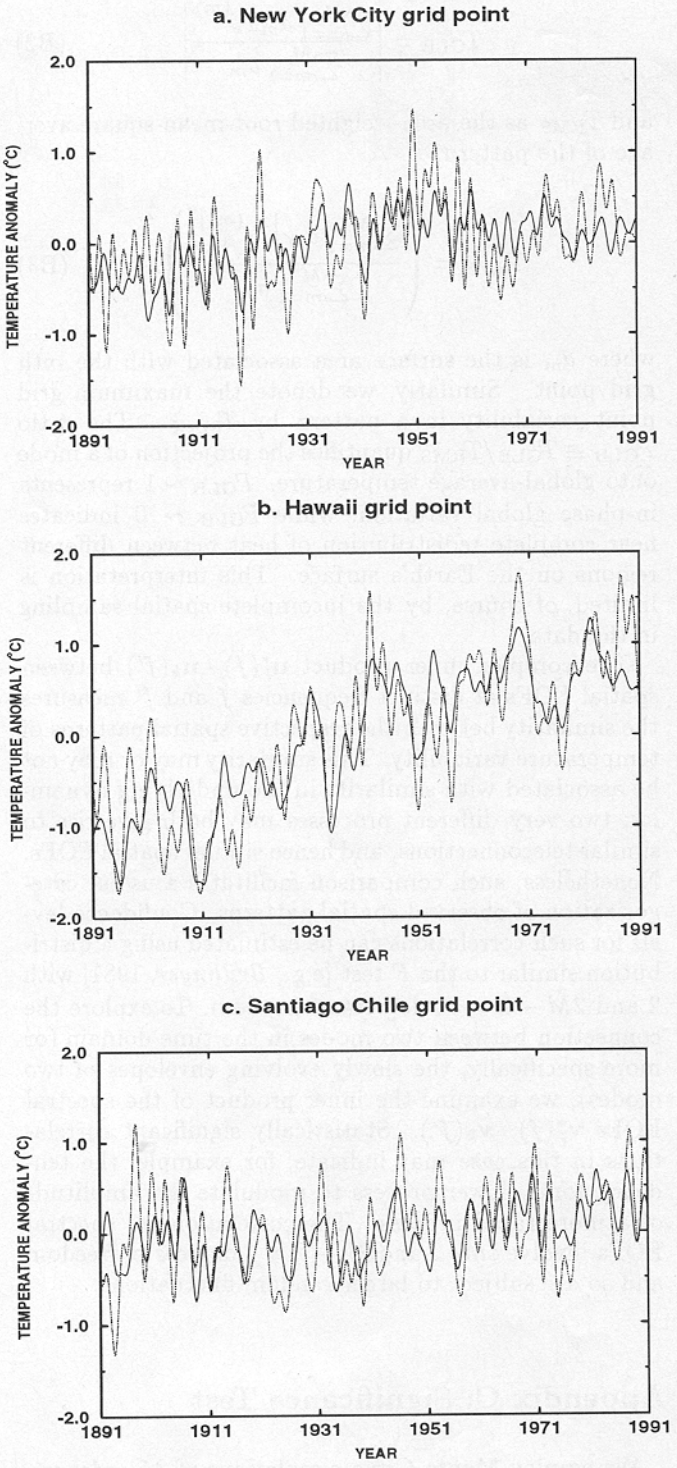

Figure 12. Time domain signals reconstructed from the 10 spatio-temporal signals isolated in the analysis (solid) along with the raw 2-year low-passed time series (dotted) for some example grid points. (a) Grid point containing New York City. The reconstruction captures the observed secular trend effectively, as well as strong quasi-biennial fluctuations. (b) Grid point containing main island of Hawaii. The time series exhibits a strong warming trend, which is captured by the secular warming mode, with interdecadal fluctuations also clearly captured. c) Grid point containing Santiago, Chile. Strong El Nino events [e.g., *Quinn and Neal*, 1992] are clearly captured in the reconstruction.

or with extratropical patterns that chiefly involve an NAO pattern. Decadal variability has weak impact on global-average temperature but gives rise to a strong redistribution of surface heat. A 15-to-18-years timescale interdecadal signal appears to be related to long-term variations in ENSO with significant amplitude and projection onto global-average temperature. This signal contributed to the anomalous warmth of the 1980s, although it produced a cooling effect in the southeast United States and northern Europe over the same period. Most of the secular variability is explained by a globally-coherent warming trend with spatial nonuniformity that may relate to regionally important feedbacks and secular changes in atmospheric circulation. The remainder of the secular variability is primarily organized on a ~100-year timescale with large variability in the high-latitude North Atlantic, but with weak projection onto global-average temperature. This latter signal may be related to long-term variability in the thermohaline circulation and cryosphere.

The fundamental limitations of the present study are the relatively short length of time series and paucity of data over much of the Earth's surface. Studies based on long-term, high-resolution climate proxy records might be used to extend the temporal scope of analysis, albeit properly with a recognition of the appreciable limitations of those data. Studies with better spatial coverage based on shorter data sets might be useful to better characterize the spatial patterns of shorter timescale processes, and investigations of joint modes of variability among multiple climate indices might provide greater physical insight. Such investigations, which should provide better constraints on the spatio-temporal structure of low-frequency climate variations, will be essential as we seek to better understand the origins and predictability of global climate variability.

Appendix A: Envelope Inversion and Signal Reconstruction

Park [1992] and *Park and Maasch* [1993] show how the slowly varying envelope $A(t)$ of a quasi-periodic signal $x(t) = \Re\{A(t)e^{-i2\pi f_0 t}\}$ centered at a "carrier" frequency f_0 can be estimated from a set of eigenspectra $Y_l(f_0)$, $l = 1, \ldots K$. The time domain signal $x(t)$ and envelope $\Re A(t)$ are formally identical for modes referenced to $f_0 = 0$, that is, the secular modes of variability. In the multivariate case the evolution of the kth mode of variability near f_0 can be reconstructed from the components of its corresponding spectral EOF $\mathbf{v}_k^*(f_0)$. This reconstruction is not unique and requires additional constraints. The simplest reconstruction is a variation of the complex demodulate, which has a closed form expression as a linear combination of the Slepian tapers $\{w_n^{(l)}\}_{n=1}^N$

$$\tilde{A}_k(n\Delta t) = \sum_{l=1}^{K} \xi_l^{-1} \lambda_l(f_0)(v_k^{(l)})^* w_n^{(l)}, \qquad \text{(A1)}$$

where $v_k^{(l)}$ is the lth component of the vector $\mathbf{v_k}(f_0)$. The ξ_l are the bandwidth retention factors of the Slepian tapers [see *Park and Maasch*, 1993]. This reconstruction tends to minimize the size of the envelope and thus favors $\tilde{A}_k \to 0$ at the ends of the time series. Such a constraint is inappropriate for secular modes centered on $f_0 = 0$, as they may be associated with nonstationary behavior in the data series. For secular modes we minimize the numerical first derivative of $\tilde{A}_k(n\Delta t)$ [*Park*, 1992], which favors envelopes that approach zero slope at the ends of the time series and does not artificially discriminate against an overall warming or cooling trend in the data. A third possible constraint would minimize the roughness of the envelope using the second derivative of $\tilde{A}_k(n\Delta t)$. Our choice of using (A1) for non secular modes and the first-derivative constraint for secular modes is justified a posteriori by the fact that this choice explains the largest fraction of the aggregate variance in the grid point time series, compared to other permutations of the constraints described above. Using the envelope estimate, the reconstructed signal $\tilde{T}$ of the kth mode of variability for the mth grid point data series near any frequency f is

$$\tilde{T}_n = \gamma(f)\Re\left\{\sigma^{(m)}u_k^{(m)}\tilde{A}_k(n\Delta t)e^{-i2\pi f n\Delta t}\right\}, \quad \text{(A2)}$$

where $u_k^{(m)}$ is the mth component of the spatial EOF $\mathbf{u}_k(f)$. The factor $\gamma(f) = 2$ for $f \gtrsim pf_R$, owing to contributions from spectral information near f and $-f$. At $f = 0$, $\gamma(f) = 1$. For $0 < f \lesssim pf_R$, the value of γ is more problematic, as the sampling widths of the Slepian tapers in the frequency domain for f and $-f$ overlap partially. In practice, it is simplest to treat such long-period variability as quasi-secular and use the $f = 0$ passband for its reconstruction.

Appendix B: Reconstruction of Spatial Patterns

In various plots we display spatial patterns of temperature variability whose (complex-valued) components

$$\hat{T}_k^{(m)} = \gamma(f)\sigma^{(m)}u_k^{(m)}A_{\mathrm{MAX}}(f) \quad \text{(B1)}$$

are represented by vectors with magnitudes proportional to temperature, and directions that indicate the relative phase between different grid points. $A_{\mathrm{MAX}}(f)$ scales the pattern by the maximum amplitude of the envelope (i.e., the maximum peak-to-peak amplitude of a particular oscillation) over the 100-years record. Unlike the associated spatial EOFs, reconstructed temperature patterns corresponding to different modes in a given frequency band do not comprise an orthonormal set. To estimate the influence of a particular mode of variability on globally averaged temperature, we define T_{GLB} as the peak-to-peak area-weighted global average of $\hat{T}_k^{(m)}$ associated with a given mode,

$$T_{\mathrm{GLB}} = \left|\frac{\sum_{m=1}^{M} a_m \hat{T}_k^{(m)}}{\sum_{m=1}^{M} a_m}\right| \quad \text{(B2)}$$

and T_{RMS} as the area-weighted root-mean-square average of the pattern,

$$T_{\mathrm{RMS}} = \left(\frac{\sum_{m=1}^{M} a_m \left|\hat{T}_k^{(m)}\right|^2}{\sum_{m=1}^{M} a_m}\right)^{\frac{1}{2}} \quad \text{(B3)}$$

where a_m is the surface area associated with the mth grid point. Similarly, we denote the maximum grid point variability in a pattern by T_{MAX}. The ratio $P_{\mathrm{GLB}} \equiv T_{\mathrm{GLB}}/T_{\mathrm{RMS}}$ quantifies the projection of a mode onto global-average temperature. $P_{\mathrm{GLB}} \sim 1$ represents in-phase global variation, while $P_{\mathrm{GLB}} \sim 0$ indicates near complete redistribution of heat between different regions on the Earth's surface. This interpretation is limited, of course, by the incomplete spatial sampling in the data.

The complex inner product $\mathbf{u}_l^*(f) \cdot \mathbf{u}_k(f')$ between spatial EOFs at distinct frequencies f and f' measures the similarity between the respective spatial patterns of temperature variability. This similarity may or may not be associated with similarity in the underlying dynamics; two very different processes may both give rise to similar teleconnections, and hence similar spatial EOFs. Nonetheless, such comparison facilitates a useful categorization of observed spatial patterns. Confidence levels for such correlations can be estimated using a distribution similar to the F test [e.g., *Brillinger*, 1981] with 2 and $2\tilde{M} - 2 = 38$ degrees of freedom. To explore the connection between two modes in the time domain (or more specifically, the slowly evolving envelopes of two modes), we examine the inner product of the spectral EOFs $\mathbf{v}_l^*(f) \cdot \mathbf{v}_k(f')$. Statistically significant correlations in this case may indicate, for example, the tendency for a slower process to modulate the amplitude of a more rapid process. The correlations of spectral EOFs involve only 2 and $2K - 2 = 4$ degrees of freedom and so are subject to larger random fluctuations.

Appendix C: Significance Test

We employ Monte Carlo simulations of $\tilde{M}$ independent Gaussian white noise time series using $K = 3, p = 2$ as in the original analysis. Since the SVD analysis is performed locally in the frequency domain within narrow frequency bands, the use of white noise time series here amounts to the weaker null hypothesis that the individual grid point time series exhibit "locally white" spectra. By "locally white" we mean that the spectrum does not vary greatly (i.e., an order of magnitude) within the narrow frequency bandwidth of the Slepian tapers we employ in our analysis. The spectra of hemisphere- and global-averaged temperature anomalies [*Jones*, 1986a, b, c] vary by nearly two orders of

magnitude between interannual and secular frequencies, because in-phase secular warming adds constructively in the spatial averages while higher-frequency variability typically cancels. The assumption of locally white series would thus be suspect in this case, at least in certain frequency bands. In contrast, the individual grid point series used in this study exhibit secular and interannual variations of comparable magnitude so that they can, with few exceptions, be described as "locally white." We only require that the variance near any given frequency f is distributed among the $K = 3$ independent spectral modes as it would be for a locally white process, rather than requiring any particular global structure in the power spectra. We regard as statistically significant any λ_k that garners a larger fraction of the total variance within the associated narrow frequency band (defined as $\lambda_k^2 / \sum_{j=k}^{K} \lambda_j^2$) than in a sufficiently large percentage of the Monte Carlo realizations. Using Slepian tapers with $p = 2$, we can partition $0 \leq f \leq 0.5$ cycle/yr into 13 nonoverlapping, and hence statistically independent, frequency bands. Thus it is probable that one primary mode in the SVD analysis would randomly exceed the 95% confidence level. Exceeding the 99% confidence level is unlikely, in the context of our null hypothesis. By testing the robustness of our analysis with respect to changes in spatial and temporal sampling, we further guard against spurious inferences. The confidence limits obtained from the Monte Carlo simulations for $\tilde{M} = 20$, and $K = 3$, $p = 2$ are summarized in Table C1. Confidence limits for $\tilde{M} = 40$ are also shown for comparison.

An alternative significance test based on a resampling technique was used as a consistency measure. In this case no assumptions were made regarding spatial degrees of freedom or the particular shape of the probability distribution function (e.g., Gaussian) of the temperature data. The monthly temperature fields were kept spatially intact, but the 1200 months were permuted into random sequences of the same length. This process should destroy preexisting frequency-dependent correlations in the data set, leaving those that persist independent of timescale. One thousand independent permutations were generated, and empirical confidence limits were determined as above. The confidence limits obtained are consistent with those obtained with a value $27 < \tilde{M} < 36$ using the first significance test described (i.e., random fluctuations of locally white Gaussian random processes). This represents a range of values of $\tilde{M}$ which are all more liberal than the value ($\tilde{M} = 20$) adopted.

Table C1. Confidence Limits for the Fractional Variance Explained by Locally White Noise Based on Monte Carlo Simulations with 3 Spectral Degrees of Freedom, and 20 Spatial and 40 Spatial Degrees of Freedom for Comparison

	EOF	Spatial DOF	90%	95%	99%
outside $f = 0$ band	1	20	0.50	0.52	0.55
outside $f = 0$ band	2	20	0.65	0.68	0.71
within $f = 0$ band	1	20	0.63	0.65	0.69
within $f = 0$ band	2	20	0.92	0.94	0.96
outside $f = 0$ band	1	40	0.46	0.47	0.49
outside $f = 0$ band	2	40	0.61	0.63	0.65
within $f = 0$ band	1	40	0.58	0.59	0.62
within $f = 0$ band	2	40	0.90	0.92	0.93

Each spatial and spectral degree of freedom possesses statistically independent real and imaginary parts. Confidence limits are higher within the band $0 < f < 0.02$ cycle/yr, owing to the fact the imaginary parts of the spectral estimates vanish near zero frequency.

Acknowledgments. We thank Tom Boden of CDIAC and Roy Jenne of NCAR for help in obtaining the temperature data sets used. Helpful comments and suggestions from B. Saltzman, U. Lall, K. Maasch, E. Bolton, and the two anonymous reviewers are gratefully acknowledged. We thank Robert Livezey for suggesting the resampling-based confidence test used. M. Mann has been supported by NASA grant NAG5-2316 and EPRI grant RP 3267-07. J. Park has been supported by NSF grant EAR-9219367.

References

Allen, M. R., Read, P. L., and L. A. Smith, Temperature time series, *Nature, 355*, 686, 1992.

Angell, J.K., Variation in global tropospheric temperature after adjustment for the El Nino influence, 1958-1989, *Geophys. Res. Lett., 17*, 1093–1096, 1990.

Barnett, T.P., The interaction of multiple time scales in the tropical climate system. *J. Clim., 4*, 269–281, 1991.

Barnston, A.G., and R.E. Livezey, Classification, seasonality and persistence of low-frequency atmospheric circulation patterns, *Mon. Weather Rev., 115*, 1083–1126, 1987.

Barnston, A.G., R.E. Livezey, and M.S. Halpert, Modulation of southern oscillation–northern hemisphere mid-winter climate relationships by the QBO, *J. Clim., 4*, 203–227, 1991.

Bjerknes, J., Atlantic air-sea interactions, *Adv. Geophys., 10*, 1–82, 1964.

Bradley, R.S., H.F. Diaz, G.N. Kiladis, and J.K. Eischeid, ENSO signal in continental temperature and precipitation records, *Nature, 227*, 497–501, 1987.

Bradley, R.S., and P.D. Jones, "Little Ice Age" summer temperature variations: Their nature and relevance to recent global warming trends, *Holocene, 3*, 367-376, 1993.

Bradley, R.S., and P.D. Jones, Records of explosive volcanic eruptions over the last 500 years, in *Climate Since A.D. 1500*, edited by R.S. Bradley and P.D. Jones, pp. 606-622, Routledge and Kegan Paul, Boston, Mass., 1992.

Briffa, K.R., and P.D. Jones, *Holocene, 3*, Surface air temperature variations during the 20th century: Part 2–Implications for large-scale high-frequency paleoclimate studies, *Holocene, 3*, 82-92, 1993.

Brillinger, D.R., *Time Series, Data Analysis and Theory*, Holden-Day, Oakland, Calif., 1981.

Cayan, D.R., and D.H. Peterson, The influence of North Pacific atmospheric circulation on streamflow in the west, in *Aspects of Climate Variability in the Pacific and the Western Americas, Geophys. Monogr. Ser.*, vol. 55, edited by D.H. Peterson, pp. 375–397, AGU, Washington, D.C., 1989.

Currie, R.G., and D.P. O'Brien, Deterministic signals in USA precipitation records; II, *Int. J. Climatol., 12*, 281–304, 1992.

Deser, C., and M. Blackmon, Analysis of decadal climate

variations over the Atlantic basin, paper presented at *5th Conference on Climate Variations*, Am. Meteorol. Soc., Denver, Colo., Oct. 14-18, 1991.

Deser, C., and M. Blackmon, Surface climate variations over the North Atlantic ocean during winter: 1900-1989, *J. Clim., 6*, 1743–1753, 1993.

Dettinger, M.D., and M. Ghil, Interannual and interdecadal variability of surface-air temperatures in the United States, in *Proceedings of the XVIth Annual Climate Diagnostics Workshop*, pp. 209-214, U.S. Department of Commerce, NOAA, Los Angeles, Calif., 1991.

Dickey, J.O., S.L. Marcus, and R. Hide, Global propagation of interannual fluctuations in atmospheric angular momentum, *Nature, 357*, 484–488, 1992.

Dickson, R.R., and J. Namias, North American influences on the circulation and climate of the North Atlantic sector, *Mon. Weather Rev., 104*, 1255–1265, 1976.

Elsner, J.B., and A.A. Tsonis, Do bidecadal oscillations exist in the global temperature record?, *Nature, 353*, 551–553, 1991.

Folland, C.K., D.E. Parker, and F.E. Kates, Worldwide marine temperature fluctuations 1856-1981, *Nature, 310*, 670–673, 1984.

Folland, C.K., T.N. Palmer, and D.E. Parker, Sahel rainfall and worldwide sea temperatures, *Nature, 320*, 602–606, 1986.

Friis-Christensen, E., and K. Lassen, Length of the solar cycle: An indicator of solar activity closely associated with climate, *Science, 254*, 698–700, 1991.

Ghil, M., and R. Vautard, Interdecadal oscillations and the warming trend in global temperature time series, *Nature, 350*, 324–327, 1991.

Gordon, A.L., S.E. Zebiak, and K. Bryan, Climate variability and the Atlantic ocean, *Eos Trans., AGU, 73*, 161-165, 1992.

Halpert, M.S., and C.F. Ropelewski, Surface temperature patterns associated with the Southern Oscillation, *J. Clim., 5*, 577–593, 1992.

Hansen, J., and S. Lebedeff, Global trends of measured surface air temperature, *J. Geophys. Res., 92*, 13345–13372, 1987.

Horel, J.D., and J.M. Wallace, Planetary-scale atmospheric phenomena associated with the Southern Oscillation, *Mon. Weather Rev., 109*, 813–829, 1981.

Houghton, R., and Y. Tourre, Characteristics of low-frequency sea-surface temperature fluctuations in the tropical Atlantic, *J. Clim., 5*, 765–771, 1992.

International Panel on Climate Control, *Climate Change, the IPCC Scientific Assessment,* edited by J.T. Houghton, G.J. Jenkins, and J.J. Ephraums, Cambridge University Press, New York, 1990.

Jones, P.D., The influence of ENSO on global temperatures, *Clim. Monit., 17*, 80-89, 1989.

Jones, P.D., and K.R. Briffa, Global surface air temperature variations during the 20th century, 1, Spatial, temporal and seasonal details, *Holocene, 1*, 165–179, 1992.

Jones, P.D., S.C. Raper, R.S. Bradley, H.F. Diaz, P.M. Kelly, and T.M. Wigley, Northern hemisphere surface air temperature variations, *J. Clim. Appl. Meteorol., 25*, 161–179, 1986a.

Jones, P.D., S.C. Raper, and T.M. Wigley, Southern hemisphere surface air temperature variations, *J. Clim. Appl. Meteorol., 25*, 1213–1230, 1986b.

Jones, P.D., T.M. Wigley, and P.B. Wright, Global temperature variation between 1861 and 1984, *Nature, 322*, 430–434, 1986c.

Julian, P.R., and H.J. Thiebaux, On some properties of correlation functions used in optimum interpolation schemes, *Mon. Weather Rev., 103*, 605–616, 1975.

Keppenne, C.L., and M. Ghil, Adaptive filtering and prediction of the Southern Oscillation index, *J. Geophys. Res., 97*, 20449–20454, 1992.

Kim, K.Y., and G.R. North, Surface temperature fluctuations in a stochastic climate model, *J. Geophys. Res., 96*, 18573–18580, 1991.

Kuo, C., C. Lindberg, and D.J. Thomson, Coherence established between atmospheric carbon dioxide and global temperature, *Nature, 343*, 709–713, 1990.

Labitzke, K., and H. van Loon, Associations between the 11–year solar cycle, the QBO, and the atmosphere, I, The troposphere and stratosphere in the northern hemisphere in winter, *J. Atmos. Terr. Phys., 50*, 197–206, 1988.

Lamb, P.J., and R.A. Peppler, North Atlantic oscillation: Concept and an application, *Bull. Am. Meteorol. Soc., 68*, 1218-1225, 1987.

Levitus, S., Interpentadel variability of temperature and salinity at intermediate depths of the North Atlantic ocean, 1970-1974 versus 1955-1959, *J. Geophys. Res., 94*, 6091–6131, 1989.

Lins, H.F., Streamflow variability in the United States, 1931–78. *J. Clim. Appl. Met., 24*, 463–471, 1985.

Livezey, R.E., and W.Y. Chen, Statistical field significance and its determination by Monte Carlo techniques, *Mon. Weather Rev., 111*, 46-59, 1983.

Lorenz, E.N., Can chaos and intransitivity lead to interannual variability?, *Tellus, 42A*, 378–389, 1990.

Madden, R.A., D.J. Shea, G.W. Branstator, J.J. Tribbia, and R.O. Weber, The effects of imperfect spatial and temporal sampling on estimates of the global mean temperature: Experiments with model data, *J. Clim., 6*, 1057–1066, 1993.

Mann, M.E., and J. Park, Spatial correlations of interdecadal variation in global surface temperatures, *Geophys. Res. Lett., 20*, 1055–1058, 1993.

Mann, M.E., and J. Park, Globally correlated variability in surface temperatures, paper presented at *6th Conference on Climate Variations*, Am. Meteorol. Soc., Nashville, Tenn., Jan. 23-28, 1994.

Marple, S.L., *Digital Spectral Analysis With Applications*, Prentice-Hall, Englewood Cliffs, N.J., 1987.

Marshall, S., M.E. Mann, R.J. Oglesby, and B. Saltzmann, A comparison of CCM1-simulated climates for pre-industrial and present-day CO_2 levels, *Global Planet. Change*, in press, 1994.

Mehta, V.M., and T. Delworth, Decadal variability in the tropical Atlantic Ocean surface temperature in shipboard measurements and a global ocean-atmosphere model, *J. Clim.*, in press, 1994.

Mitra, K., S. Mukherji, and S.N. Dutta, Some indications of 18.6 year luni-solar and 10-11 year solar cycles in rainfall in northwest India, the plains of Uttar Pradesh and north-central India, *Int. J. Climatol., 11*, 645–652, 1991.

Mysak, L.A., and S.B. Power, Sea-ice anomalies in the western Arctic and Greenland-Iceland Sea and their relation to an interdecadal climate cycle, *Climatol. Bull., 26*, 147–176, 1992.

Palecki, M.A., and D.J. Leathers, Northern hemisphere extratropical circulation anomalies and recent January land surface temperature trends, *Geophys. Res. Lett., 20*, 819–822, 1993.

Palmer, T.N., Extended-range atmospheric prediction and the Lorenz model, *Bull. Am. Meteorol. Soc., 74*, 49–65, 1993.

Park, J., Envelope estimation for quasi-periodic geophysical signals in noise: A multitaper approach, in *Statistics in the Environmental and Earth Sciences*, edited by A. T. Walden and P. Guttorp, pp. 189–219, Edward Arnold, London, 1992.